

# Encapsulation of Molybdenum Carbide Nanoclusters inside Zeolite Micropores Enables Synergistic Bifunctional Catalysis for Anisole Hydrodeoxygenation

Takayuki Iida,<sup>†,‡</sup> Manish Shetty,<sup>‡</sup> Karthick Murugappan,<sup>‡</sup> Zhenshu Wang,<sup>‡</sup> Koji Ohara,<sup>§</sup> Toru Wakihara,<sup>\*,†</sup> and Yuriy Román-Leshkov<sup>\*,‡</sup>

<sup>†</sup>Department of Chemical System Engineering, The University of Tokyo, 7-3-1 Hongo, Bunkyo-ku, Tokyo 113-8656, Japan

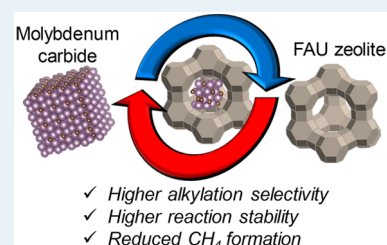
<sup>‡</sup>Department of Chemical Engineering, Massachusetts Institute of Technology, 25 Ames Street, Cambridge, Massachusetts 02139, United States

<sup>§</sup>Japan Synchrotron Radiation Research Institute/SPring-8, Kouto 1-1-1, Sayo-gun, Hyogo 679-5198, Japan

## Supporting Information

**ABSTRACT:** Molybdenum carbide ( $\text{MoC}_x$ ) nanoclusters were encapsulated inside the micropores of aluminosilicate FAU zeolites to generate highly active and selective bifunctional catalyst for the hydrodeoxygenation of anisole. Interatomic correlations obtained with differential pair distribution function analysis confirmed the intraparticle structure and the uniform size of the  $\text{MoC}_x$  nanoclusters. The reactivity data showed the preferential production of alkylated aromatics (such as toluene and xylene) over benzene during the hydrodeoxygenation of anisole as well as the minimization of unwanted  $\text{CH}_4$  formation. Control experiments demonstrated the importance of  $\text{MoC}_x$  encapsulation to generate an efficient bifunctional catalyst with superior carbon utilization and on-stream stability.

**KEYWORDS:** hydrodeoxygenation, bifunctional catalyst, zeolite encapsulation, molybdenum carbide, pair distribution function



Bifunctional catalysts have been reported to open up remarkable reaction routes to desired products at high yields in multistep reactions.<sup>1</sup> Metal-supported zeolites are promising materials for acid/metal bifunctional catalysis, as exemplified in the simultaneous Fischer–Tropsch/hydrocracking,<sup>2</sup> as well as in the hydroisomerization of alkanes<sup>3</sup> using cobalt<sup>2</sup> and platinum<sup>3</sup> metals supported on zeolites, respectively. The efficient combination of zeolite pore confinement effects with nanoparticles having unconventional redox-active sites, such as transition-metal carbides, will provide further possibilities for developing new bifunctional catalysts. For some reactions, early transition-metal carbides have shown similar catalytic activity to that of group VIII noble metals,<sup>4</sup> and are gaining more attention in applications such as electrocatalysis,<sup>5,6</sup> hydrodeoxygenation,<sup>7,8</sup> and Fischer–Tropsch chemistry.<sup>9,10</sup> Indeed, various transition-metal carbides supported on ZSM-5 zeolites are the preferred catalysts for methane dehydroaromatization.<sup>11–13</sup>

The efficient bifunctionality of these materials hinges on the molecular proximity of the metallic sites of the nanoparticles with the Brønsted acid sites of the zeolites.<sup>2,13</sup> Therefore, the controlled synthesis and detailed characterization of the encapsulated metallic species (usually <1 nm in diameter) is of critical importance to direct targeted reaction pathways. A major bottleneck for achieving these goals lies in the lack of methodologies for understanding the structural nature of the metallic nanoclusters, such as the particle size distribution and atomic-scale intraparticle structure. The limited loadings

(usually ~1 wt %) and the small particle sizes prevent the use of conventional analytical techniques such as powder X-ray diffraction (PXRD).<sup>14</sup> Similarly, while transmission electron microscopy (TEM) can provide information regarding the particle size and morphology, other structural information is limited. Extended X-ray absorption fine structure (EXAFS)<sup>15</sup> and chemisorption<sup>16</sup> are powerful tools in characterizing nanoclusters composed of single metallic element, providing information regarding crystal structure and particle size, but the accurate interpretation of these measurements becomes more challenging for heterometallic nanoparticles. For example, CO chemisorption values on a carbide are highly dependent on synthesis conditions and the nature of the surface (e.g., mild passivation or presence of coke),<sup>17,18</sup> and thereby, dispersion measurements may provide inaccurate results. The development of reliable characterization tools for carbide nanoclusters is critical for the design and implementation of these materials in various catalytic processes.

In this work, we first encapsulated molybdenum carbide ( $\text{MoC}_x$ ) nanoclusters within the pores of zeolites with the faujasite (FAU) topology and then used pair distribution function (PDF) analysis to conduct a detailed characterization of their structures. While the formation of  $\text{MoC}_x$  species inside

Received: September 16, 2017

Revised: October 16, 2017

Published: October 20, 2017

the zeolites pores has been demonstrated in prior studies,<sup>11–13</sup> their particle size distribution and intraparticle atomic arrangement have remained ambiguous.<sup>19</sup> PDF represents the probability of finding an interatomic distance inside an unit volume, and has conventionally been used to describe disordered structures that are not amenable to conventional diffraction techniques (e.g., amorphous vitreous glasses).<sup>20</sup> The availability of this method for describing structural arrangements at distances beyond those reliably quantifiable by EXAFS (>5 Å) has allowed the acquisition of information on other crystalline nanostructures including heterometallic nanoparticles<sup>21,22</sup> and even disorders in bulk crystals.<sup>23</sup> We investigated the encapsulated MoC<sub>x</sub> nanoclusters as catalysts for the vapor phase hydrodeoxygenation (HDO) of anisole, a biomass-based model compound with methoxybenzene motif prevalent in lignin's structure.<sup>24,25</sup> The use of pristine molybdenum carbide (Mo<sub>2</sub>C) catalysts for these reactions has been shown to produce benzene and methane as the main products with high selectivity and minimal formation of ring-saturated by-products.<sup>25</sup> Zeolites are known to be effective deoxygenation agents for pyrolysis oil, at the expense of producing large amounts of coke.<sup>26</sup> We show that the bifunctional MoC<sub>x</sub>/FAU catalyst displayed stable (trans)alkylation and hydrodeoxygenation activity, generating a high proportion of alkylated aromatics (alkylated aromatics/benzene ratio ~2.9 C-mol %), while minimizing the formation of undesirable products, namely methane, due to close interaction between strong zeolitic Brønsted acid sites and carbidic metallic sites (Figure 1).

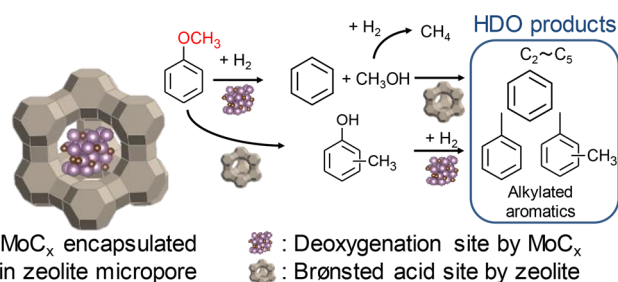


**Figure 1.** Bifunctional anisole conversion by MoC<sub>x</sub> encapsulated FAU zeolite catalyst for producing alkylated aromatics and C<sub>2</sub>~C<sub>5</sub> light gas elements by the combination of zeolitic Brønsted acid sites and MoC<sub>x</sub> deoxygenation sites.

The MoC<sub>x</sub>/FAU catalysts were synthesized by solid state ion exchange of Mo<sup>6+</sup> with (NH<sub>4</sub>)<sub>6</sub>Mo<sub>7</sub>O<sub>24</sub>·4H<sub>2</sub>O followed by a carburization treatment under CH<sub>4</sub> and H<sub>2</sub> flow at 973 K. The Si/Al ratio of the zeolite was 15, and the Mo/Al ratio was fixed to 0.5, resulting in a Mo loading of 5 wt %. Pristine Mo<sub>2</sub>C was prepared by carburization of (NH<sub>4</sub>)<sub>6</sub>Mo<sub>7</sub>O<sub>24</sub>·4H<sub>2</sub>O at 923 K for 3 h. Detailed catalyst preparation procedures are summarized in the [Supporting Information](#).

As expected, conventional PXRD patterns associated with Mo<sub>2</sub>C were not detected in the MoC<sub>x</sub>/FAU samples (Figure S1). Therefore, structural characterization of MoC<sub>x</sub> species was performed using differential pair distribution function (d-PDF),<sup>22,27</sup> an applied form of PDF analysis useful for determining specific phases in binary mixtures. This technique involves taking the difference between the pair distribution functions,  $G(r)$ , of the mixture and the admixed secondary phase as shown in eqs 1 and 1' below:

$$G_{A+B}(r) \cong x_A G_A(r) + x_B G_B(r) \dots \quad (1)$$

$$x_A G_A(r) \cong G_{A+B}(r) - x_B G_B(r) \dots \quad (1')$$

where A and B represent specific phases (in this case A represents the MoC<sub>x</sub> phase and B represents the FAU zeolite phase, A + B represents the mixture of the two phases, and  $x_A$  and  $x_B$  are coefficients). The calculated d-PDF result for MoC<sub>x</sub>/FAU is shown in Figure 2A, and that for the physical mixture of

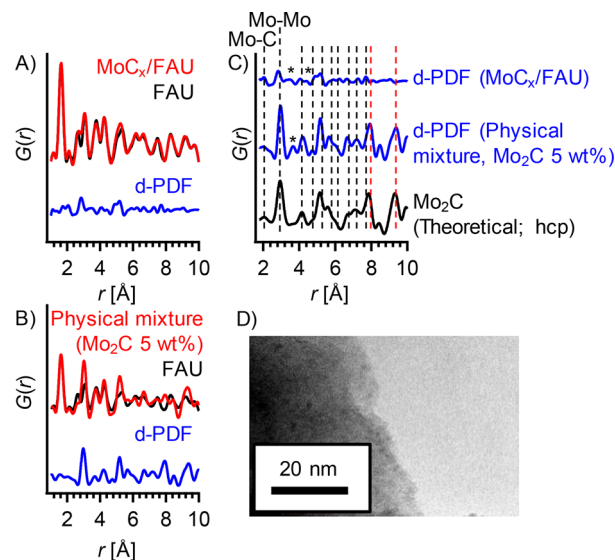


**Figure 2.** (A) Pair distribution function,  $G(r)$ , of MoC<sub>x</sub>/FAU, parent FAU and calculated d-PDF of occluded MoC<sub>x</sub> element, (B) Pair distribution function,  $G(r)$ , of a physical mixture of Mo<sub>2</sub>C and FAU (5 wt % Mo), parent FAU and calculated d-PDF of Mo<sub>2</sub>C element, (C) Comparison of d-PDF results with the simulated pair distribution function,  $G(r)$ , of Mo<sub>2</sub>C (hcp phase) using PDFgui software,<sup>28</sup> and (D) Typical TEM image of MoC<sub>x</sub>/FAU. Correlations corresponding to Mo<sub>2</sub>C are shown with dotted lines, and the correlations assigned to MoO<sub>x</sub> species are marked with an asterisk(\*).

Mo<sub>2</sub>C and FAU zeolite with equivalent Mo weight loading is shown in Figure 2B. To account for the correlation peaks, the theoretical  $G(r)$  of Mo<sub>2</sub>C (hcp phase) was calculated using PDFgui software<sup>28</sup> and is shown in Figure 2C for comparison. Ziman–Faber total structure factors,  $S(Q)$ , used for the calculation of the PDFs are summarized in Figure S2. Correlations corresponding to the Mo<sub>2</sub>C phase were observed up to  $r \sim 7$  Å for MoC<sub>x</sub>/FAU (shown with black dotted lines), but were not observed at longer distances (shown with red dotted lines) showing that the nanoclusters only possess structural ordering up to around 7 Å, corresponding to no larger than three unit cells. On the contrary, the d-PDF of the physical mixture possessed correlations ranging beyond this distance, confirming that if a bulk structure had formed, all the theoretical correlations in this distance range should be apparent. Thus, these data are in agreement with the presence of  $\sim 10$  Å sized nanoclusters as observed in the TEM images shown in Figure 2D. Assignment of the correlation peaks in Mo<sub>2</sub>C were made using the PDFgui software,<sup>28</sup> and most visible correlations were found to originate from either the Mo–C (at 2.0 Å) or the Mo–Mo correlations (other correlations shown with dotted lines) due to the relatively large X-ray scattering factor by Mo compared to C (Figure S3). Further, correlations corresponding to the hcp Mo<sub>2</sub>C phase were confirmed in the d-PDF of the physical mixture wherein

standalone bulk Mo<sub>2</sub>C species are present outside of the zeolite crystal.

The PDF analysis of the MoC<sub>x</sub>/FAU material showed correlations that did not belong to the Mo<sub>2</sub>C phase at  $r = 3.3$  and  $4.4 \text{ \AA}$  (shown with asterisks\*). A comparison with various control materials including bcc Mo(0), MoO<sub>2</sub>, and MoO<sub>3</sub> (Figure S4) confirmed that the observed peaks match those of MoO<sub>x</sub> species, which are likely located on the surface of the carbide as a passivation layer. The absence of correlation peaks at  $r = 2.7$  and  $3.2 \text{ \AA}$  corresponding to Mo(0) (bcc) denoted that any metallic molybdenum species present in the sample were below the detection limit. These data are in agreement with X-ray photoelectron spectroscopy (XPS) data probing molybdenum oxidation states of surface passivated MoC<sub>x</sub>/FAU at the Mo 3d band that showed similar amounts of Mo<sup>2+</sup> species compared to those of a surface-passivated bulk Mo<sub>2</sub>C sample (Figure S5). A PDF comparison with the orthorhombic Mo<sub>2</sub>C and  $\alpha$ -MoC<sub>1-x</sub> phases showed that distinguishing the hcp phase from the orthorhombic Mo<sub>2</sub>C phase is difficult through PDF analysis due to the high similarity in the peak positions of the two phases (as is the case with PXRD<sup>8</sup>), whereas the presence of  $\alpha$ -MoC<sub>1-x</sub> phase can be tentatively ruled out by comparing the number of peaks between  $r = 5.8$ – $6.2 \text{ \AA}$  (Figure S6). Since it is difficult to unambiguously assign the stoichiometry of the nanocluster and since it is not possible to assign a crystal structure to a solid that does not possess diffraction patterns, the term MoC<sub>x</sub> is used herein to describe these moieties. The N<sub>2</sub> physisorption data revealed a decrease in micropore volume from 0.24 (FAU) to 0.21 cc g<sup>-1</sup> (MoC<sub>x</sub>/FAU), which is consistent with the encapsulation of MoC<sub>x</sub> nanoclusters in the zeolite micropores (Figure S7, and Table S3). Taken together, our data imply that phase-pure MoC<sub>x</sub> nanoclusters of  $\sim 1 \text{ nm}$  in size were effectively encapsulated within the pores of FAU. Clearly, the capability of PDF analyses to extract structural information up to 10  $\text{\AA}$  is essential for describing the architecture of the encapsulated MoC<sub>x</sub> nanoclusters. To the best of our knowledge, this work represents the first example of a pair distribution function analysis applied for the structural characterization of transition-metal carbide nanoclusters.

MoC<sub>x</sub>/FAU was used for the coupled HDO and alkylation of anisole with the aim of obtaining a higher selectivity to alkylated arenes (e.g., toluene and xylene) in place of the benzene/methane mixture traditionally obtained with bulk Mo<sub>2</sub>C catalysts. The reaction was performed at 523 K, with  $P_{\text{Total}} = 1.013 \text{ bar}$ ,  $P_{\text{anisole}} = 0.0079 \text{ bar}$  and balance H<sub>2</sub>, under the absence of external and internal diffusion limitations (detailed experimental conditions are summarized in the SI). The product distribution consisted of benzene, toluene, alkylated aromatics C<sub>8+</sub> (i.e., ethylbenzene, xylenes, and other deoxygenated aromatics with more than eight carbons), phenol, alkylated phenols (i.e., phenolic compounds with more than seven carbon atoms), alkylated anisoles (e.g., methyl anisole), and light gas C<sub>5</sub> (i.e., aliphatic hydrocarbons with carbon numbers between one and five such as methane and ethane). To understand the role of carbide encapsulation and its synergy with acid sites, control reactions were also performed using a pristine Mo<sub>2</sub>C sample, a parent FAU zeolite, and a physical mixture of Mo<sub>2</sub>C and FAU zeolite with identical metal and/or Brønsted acid site loadings (designated as Mo<sub>2</sub>C+FAU; site count was performed by CO chemisorption and NH<sub>3</sub>-TPD, respectively, and the results are summarized in Table S4). To assess the effectiveness of MoC<sub>x</sub>/FAU catalysts on the

formation of alkylated aromatics in comparison to benzene, the alkylation ratio was defined as follows:

$$\text{alkylation ratio} = \frac{\sum \text{produced alkylated aromatics [C - mol\%]}}{\text{produced benzene [C - mol\%]}}$$

All the carbide catalysts used were carburized in situ at 973 K under a CH<sub>4</sub>/H<sub>2</sub> atmosphere before the reaction to avoid the formation of an oxide passivation layer prior to the introduction of the feed.

For all the catalysts, the conversion (Figure 3) and the product selectivity values (Figure S8–S11) reached steady state

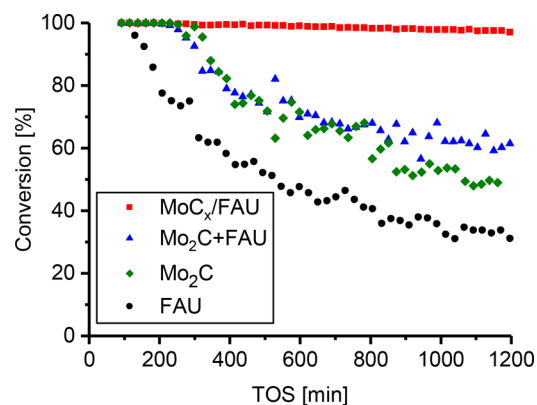


**Figure 3.** Conversion time profile of anisole over MoC<sub>x</sub>/FAU, pristine Mo<sub>2</sub>C, parent FAU, and Mo<sub>2</sub>C+FAU catalysts. All catalysts possess same metal and/or Brønsted acid site loadings. Reaction conditions: Reaction temperature: 523 K, Anisole feed: 150  $\mu\text{L/h}$ , Catalyst loading: 750 mg for MoC<sub>x</sub>/FAU, 322 mg for Mo<sub>2</sub>C, 600 mg for parent FAU, 922 mg for Mo<sub>2</sub>C+FAU,  $P_{\text{Total}} = 1.013 \text{ bar}$ ,  $P_{\text{anisole}} = 0.0079 \text{ bar}$ , and balance H<sub>2</sub>.

after ca. 1000 min on stream. Note that under identical reaction conditions and similar number of active sites, the MoC<sub>x</sub>/FAU catalyst maintained high conversions, typically above  $\sim 97\%$ , whereas the conversion of Mo<sub>2</sub>C+FAU settled around  $\sim 61\%$  after 1200 min of reaction after reaching steady state. These results imply that the encapsulated catalyst features higher apparent reactivity and stability.

The product distribution was significantly different across all samples (Figure 4). For MoC<sub>x</sub>/FAU, a significant amount of alkylated aromatics was observed, with an alkylation ratio of 2.9 based on a yield of 17 C-mol % for alkylated products vs 5.8 C-mol % for benzene. This value was maintained throughout the duration of the experiment. In contrast, the experiment using the FAU zeolite generated exclusively phenols and alkylated anisoles, both of which are products formed by (trans)-alkylation reaction catalyzed by the Brønsted acid sites of the zeolites, thus showing the lack of HDO reactivity by parent zeolite catalyst. This observation confirms that MoC<sub>x</sub> species are responsible for the HDO reactivity. Bifunctional catalysis by different materials has been performed for anisole HDO reactions,<sup>29–33</sup> with maximum alkylation ratios only  $\sim 1.8$  (MoO<sub>3</sub>/ZrO<sub>2</sub>).<sup>33</sup> Evidently, the MoC<sub>x</sub>/FAU catalyst is a highly effective bifunctional catalyst with enhanced HDO/alkylation performance over current state of the art catalysts for anisole upgrading. While the Mo<sub>2</sub>C+FAU mixture also formed alkylated aromatics as products, the alkylation ratio only reached a value of 0.47, which is on par with other bifunctional

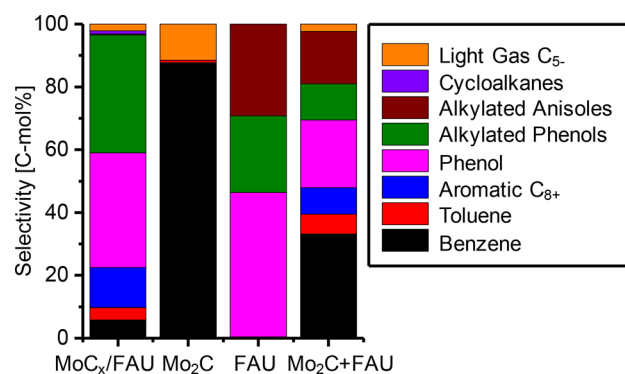


**Figure 4.** Reaction selectivity of MoC<sub>x</sub>/FAU, pristine Mo<sub>2</sub>C, parent FAU, and Mo<sub>2</sub>C+FAU catalysts at the final point of reaction run (TOS = 1200 min). The conversions of these catalysts were 97% (MoC<sub>x</sub>/FAU), 49% (Mo<sub>2</sub>C), 31% (FAU), and 61% (Mo<sub>2</sub>C+FAU). Reaction conditions are identical to those described in Figure 2. Aromatics C<sub>8+</sub> include ethylbenzene, xylenes, and the other deoxygenated aromatics having more than eight carbons. Alkylated phenols include phenolic compounds with more than seven carbon atoms such as cresols. Alkylated anisoles include substituted anisoles with more than eight carbon atoms such as methyl anisole. Light gas C<sub>5</sub> includes aliphatic hydrocarbons with carbon numbers between one and five such as methane and ethane.

catalysts.<sup>29–33</sup> The product selectivity to alkylated anisoles was significantly higher for Mo<sub>2</sub>C+FAU (20 C-mol %) than for MoC<sub>x</sub>/FAU (0.3 C-mol %). The formation of alkylated aromatics can clearly be attributed to the transalkylation of methoxy groups from one anisole molecule to another by the Brønsted acid sites. The prompt deoxygenation of the alkylated anisole species is enabled by the molybdenum carbide species in close vicinity of the Brønsted acid sites for MoC<sub>x</sub>/FAU, whereas this is not the case for Mo<sub>2</sub>C+FAU, which has a significantly longer physical distance between the two sites, allowing the desorption of these intermediate species before the subsequent deoxygenation step. It should be noted that the binding energy of C–O bond in anisole was reported to be lower in comparison to that of C–O bond in phenol,<sup>31</sup> and we hypothesize that this difference is likely the key factor for the selective deoxygenation of the (alkylated) anisole intermediate species by MoC<sub>x</sub>/FAU compared to phenols.

Remarkably, when using the bifunctional MoC<sub>x</sub>/FAU materials, methane formation was severely hindered (0.2 C-mol % in selectivity), while C<sub>2</sub>~C<sub>5</sub> hydrocarbons (~2.6 C-mol % selectivity in total) was confirmed inside the light gas C<sub>5</sub> fraction (Figure 5A). This result is in stark contrast to bulk Mo<sub>2</sub>C catalysts, which showed selectivity values of 12 C-mol % to methane.<sup>25</sup> The reaction pathway to generate C<sub>2</sub>~C<sub>5</sub> light gas elements was investigated by monitoring the aliphatic carbon/benzene ring molar ratio throughout the reaction. We note that since the aim of the calculation was to elucidate the origin of C<sub>2</sub>~C<sub>5</sub> elements, cyclohexanes were lumped into the aromatics portion because they are produced by the hydrogenation of the aromatic rings. As seen in Figure 5B, the aliphatic carbon/benzene ring molar ratio was approximately 1 throughout the entire reaction, thereby suggesting that the C<sub>2</sub>~C<sub>5</sub> light gas elements were not produced from hydrogenation/hydrocracking. Instead, C<sub>2</sub>~C<sub>5</sub> light gases are likely formed from C–C coupling reactions of anisole-derived methanol intermediates via methanol-to-olefin pathways at the zeolite acid sites.

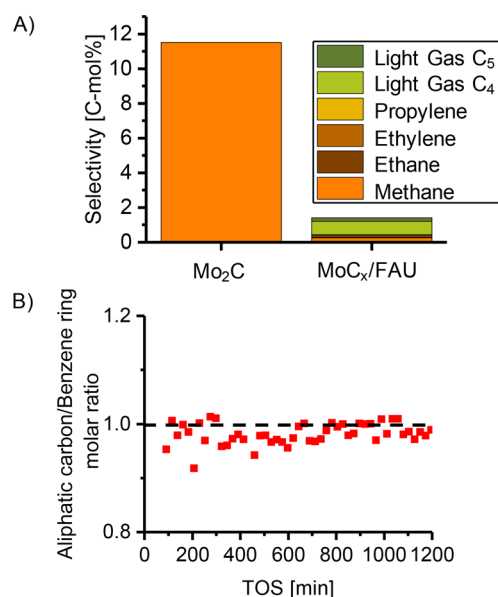


**Figure 5.** (A) Final product selectivity (TOS = 1200 min) among the light gas C<sub>5</sub> products (conversion = 97% for MoC<sub>x</sub>/FAU; conversion = 49% for Mo<sub>2</sub>C). (B) Calculated results for aliphatic carbon/benzene ring molar balance throughout the reaction run for MoC<sub>x</sub>/FAU. Reaction conditions identical to those described in Figure 3.

The fate of methoxy groups during the reaction with MoC<sub>x</sub>/FAU catalysts should result in two distinct reaction routes, namely: (1) hydrodeoxygenation via benzene ring-oxygen bond cleavage by MoC<sub>x</sub> nanoclusters followed by alkylation of the aromatic ring by the intermediate methoxy group; and (2) transalkylation of the methoxy group to the aromatic ring followed by the deoxygenation of the phenolic hydroxy group. To realize such tandem reaction pathways, the presence of both the selective deoxygenation sites of molybdenum carbide nanoclusters and the strong Brønsted acid sites of zeolites are required.

Nanocluster agglomeration in MoC<sub>x</sub>/FAU during the reaction was ruled out from post-reaction TEM images showing similar particle sizes as those observed before reaction (Figure S12). Also, the deactivation of MoC<sub>x</sub>/FAU was investigated with an experiment using a reduced catalyst loading (1/3 of the original loading) to operate at conversion values under 100% (Figure S13). At these conditions, the catalyst featured two deactivation profiles: one during the transient period (TOS < 400 min), followed by a more gradual one thereafter. Notably, the catalyst was fully regenerated by a hydrogen treatment at 773 K for 4 h, thus confirming that the observed deactivation was reversible and also ruling out irreversible nanocluster sintering. TGA measurements revealed the presence of 8.6 wt % of carbon deposits relative to the catalyst mass, pointing at coking as a possible deactivation mode. Although XPS did not show bulk oxidation of the MoC<sub>x</sub> nanoclusters even after exposure to air at room temperature, we cannot rule out the formation of an oxycarbide layer during reaction.

In summary, d-PDF analyses confirmed that our MoC<sub>x</sub>/FAU catalysts featured molybdenum carbide nanoclusters with diameters of ~1 nm that were encapsulated within the pores of FAU zeolite with high uniformity. This material effectively generated alkylated aromatics (alkylation ratio: 2.9) from the coupled HDO and alkylation of anisole, while simultaneously preventing the formation of methane byproducts (0.2 C-mol

%) in comparison to the pristine Mo<sub>2</sub>C catalyst (12 C-mol %). From the control experiments, the close proximity of the Brønsted acid sites around the metallic sites was found to be the key factor for enabling such reaction selectivity values and for increasing on-stream stability. The current findings not only suggest the existence of important advantages from having transition-metal carbide nanoclusters inside zeolite structure for catalytic applications in HDO processes, but also open up new avenues for other chemical reactions that require the bifunctionality of metallic and acidic sites.

## ■ ASSOCIATED CONTENT

### 📄 Supporting Information

The Supporting Information is available free of charge on the ACS Publications website at DOI: 10.1021/acscatal.7b03175.

PXRD patterns, further d-PDF analysis results, XPS spectra, BET specific surface areas, micropore volumes, Ziman-Faber total structure factor,  $S(Q)$ , used for calculating the pair distribution functions,  $G(r)$ , selectivity time profile of various catalysts, evaluation of external and internal mass transfer, TEM image of catalyst after reaction (PDF)

## ■ AUTHOR INFORMATION

### Corresponding Authors

\*E-mail: wakihara@chemsys.t.u-tokyo.ac.jp.

\*E-mail: yroman@mit.edu.

### ORCID

Manish Shetty: 0000-0002-8611-7415

Toru Wakihara: 0000-0002-3916-3849

Yuriy Román-Leshkov: 0000-0002-0025-4233

### Notes

The authors declare no competing financial interest.

## ■ ACKNOWLEDGMENTS

This work was supported by the U.S. Department of Energy, Office of Basic Energy Sciences under Award No. DE-SC0016214. The High Energy Total X-ray Scattering experiments conducted at SPring-8 were approved by the Japan Synchrotron Radiation Research Institute (Proposal Nos. 2015B0115 and 2016A0115). T.I. thanks the Japan Society for the Promotion of Science for a Grant-in-aid for Scientific research, and the Program for Leading Graduate Schools, “Global Leader Program for Social Design and Management (GSDM)”, by the Ministry of Education, Culture, Sports, Science and Technology, for the financial support. M.S. and K.M. acknowledge financial support from BP.

## ■ REFERENCES

- (1) Jiao, F.; Li, J. J.; Pan, X. L.; Xiao, J. P.; Li, H. B.; Ma, H.; Wei, M. M.; Pan, Y.; Zhou, Z. Y.; Li, M. R.; Miao, S.; Li, J.; Zhu, Y. F.; Xiao, D.; He, T.; Yang, J. H.; Qi, F.; Fu, Q.; Bao, X. H. *Science* **2016**, *351*, 1065–1068.
- (2) Sartipi, S.; Makkee, M.; Kapteijn, F.; Gascon, J. *Catal. Sci. Technol.* **2014**, *4*, 893–907.
- (3) Guisnet, M. *Catal. Today* **2013**, *218–219*, 123–134.
- (4) Levy, R. B.; Boudart, M. *Science* **1973**, *181*, 547–549.
- (5) Esposito, D. V.; Hunt, S. T.; Kimmel, Y. C.; Chen, J. G. *J. Am. Chem. Soc.* **2012**, *134*, 3025–3033.
- (6) Hunt, S. T.; Milina, M.; Alba-Rubio, A. C.; Hendon, C. H.; Dumesic, J. A.; Roman-Leshkov, Y. *Science* **2016**, *352*, 974–978.

- (7) Xiong, K.; Yu, W.; Vlachos, D. G.; Chen, J. G. *ChemCatChem* **2015**, *7*, 1402–1421.
- (8) Sullivan, M. M.; Chen, C. J.; Bhan, A. *Catal. Sci. Technol.* **2016**, *6*, 602–616.
- (9) Santos, V. P.; Wezendonk, T. A.; Jaen, J. J. D.; Dugulan, A. I.; Nasalevich, M. A.; Islam, H. U.; Chojecki, A.; Sartipi, S.; Sun, X.; Hakeem, A. A.; Koeken, A. C. J.; Ruitenbeek, M.; Davidian, T.; Meima, G. R.; Sankar, G.; Kapteijn, F.; Makkee, M.; Gascon, J. *Nat. Commun.* **2015**, *6*, 6451.
- (10) Zhong, L. S.; Yu, F.; An, Y. L.; Zhao, Y. H.; Sun, Y. H.; Li, Z. J.; Lin, T. J.; Lin, Y. J.; Qi, X. Z.; Dai, Y. Y.; Gu, L.; Hu, J. S.; Jin, S. F.; Shen, Q.; Wang, H. *Nature* **2016**, *538*, 84–87.
- (11) Borry, R. W.; Kim, Y. H.; Huffsmith, A.; Reimer, J. A.; Iglesia, E. *J. Phys. Chem. B* **1999**, *103*, 5787–5796.
- (12) Li, W.; Meitzner, G. D.; Borry, R. W.; Iglesia, E. *J. Catal.* **2000**, *191*, 373–383.
- (13) Kosinov, N.; Coumans, F. J. A. G.; Uslamin, E. A.; Wijkema, A. S. G.; Mezari, B.; Hensen, E. J. M. *ACS Catal.* **2017**, *7*, 520–529.
- (14) Farrusseng, D.; Tuel, A. *New J. Chem.* **2016**, *40*, 3933–3949.
- (15) Alexeev, O.; Gates, B. C. *Top. Catal.* **2000**, *10*, 273–293.
- (16) Hammer, B.; Morikawa, Y.; Norskov, J. K. *Phys. Rev. Lett.* **1996**, *76*, 2141–2144.
- (17) Lee, W.; Kumar, A.; Wang, Z.; Bhan, A. *ACS Catal.* **2015**, *5*, 4104–4114.
- (18) Oyama, S. T. *Catal. Today* **1992**, *15*, 179–200.
- (19) Gao, J.; Zheng, Y.; Fitzgerald, G. B.; de Joannis, J.; Tang, Y.; Wachs, I. E.; Podkolzin, S. G. *J. Phys. Chem. C* **2014**, *118*, 4670–4679.
- (20) Proffen, T.; Billinge, S. J. L.; Egami, T.; Louca, D. Z. *Kristallogr. - Cryst. Mater.* **2003**, *218*, 132–143.
- (21) Billinge, S. J.; Kanatzidis, M. G. *Chem. Commun.* **2004**, 749–760.
- (22) Chupas, P. J.; Chapman, K. W.; Chen, H. L.; Grey, C. P. *Catal. Today* **2009**, *145*, 213–219.
- (23) Petkov, V.; Jeong, I.-K.; Chung, J. S.; Thorpe, M. F.; Kycia, S.; Billinge, S. J. L. *Phys. Rev. Lett.* **1999**, *83*, 4089–4092.
- (24) Anderson, E. M.; Stone, M. L.; Katahira, R.; Reed, M.; Beckham, G. T.; Román-Leshkov, Y. *Joule* **2017**, DOI: 10.1016/j.joule.2017.10.004.
- (25) Lee, W. S.; Wang, Z.; Wu, R. J.; Bhan, A. *J. Catal.* **2014**, *319*, 44–53.
- (26) Jae, J.; Tompsett, G. A.; Foster, A. J.; Hammond, K. D.; Auerbach, S. M.; Lobo, R. F.; Huber, G. W. *J. Catal.* **2011**, *279*, 257–268.
- (27) Chapman, K. W.; Chupas, P. J.; Kepert, C. J. *J. Am. Chem. Soc.* **2005**, *127*, 11232–11233.
- (28) Farrow, C. L.; Juhas, P.; Liu, J. W.; Bryndin, D.; Božin, E. S.; Bloch, J.; Proffen, T.; Billinge, S. J. L. *J. Phys.: Condens. Matter* **2007**, *19*, 335219.
- (29) Zhu, X. L.; Lobban, L. L.; Mallinson, R. G.; Resasco, D. E. *J. Catal.* **2011**, *281*, 21–29.
- (30) Foo, G. S.; Rogers, A. K.; Yung, M. M.; Sievers, C. *ACS Catal.* **2016**, *6*, 1292–1307.
- (31) Prasomsri, T.; Shetty, M.; Murugappan, K.; Román-Leshkov, Y. *Energy Environ. Sci.* **2014**, *7*, 2660–2669.
- (32) Anderson, E.; Crisci, A.; Murugappan, K.; Roman-Leshkov, Y. *ChemSusChem* **2017**, *10*, 2226–2234.
- (33) Shetty, M.; Murugappan, K.; Green, W. H.; Roman-Leshkov, Y. *ACS Sustainable Chem. Eng.* **2017**, *5*, 5293–5301.